ATLAS NOTE
ATLAS-CONF-2016-095
1st September 2016

Pursuit of new phenomena in final states with high jet multiplicity, high jet masses and missing transverse momentum with ATLAS at $\sqrt{s} = 13$ TeV

The ATLAS Collaboration

Abstract

Results are reported of a search for new phenomena — such as supersymmetric particle production — that could be observed in high-energy proton-proton collisions. Events with large numbers of jets, together with missing transverse momentum from unobserved particles, are selected. The data analysed were recorded by the ATLAS experiment during 2015 and early 2016 using the 13 TeV centre-of-mass proton-proton collisions at the Large Hadron Collider, and correspond to an integrated luminosity of 18.2 fb^{-1}. The search selects events with various jet multiplicities from ≥ 8 up to ≥ 10 jets, and with various requirements on the sum of masses of large-radius reclustered jets. No excess above Standard Model expectations is observed. The results are interpreted within two supersymmetry models, where gluino masses up to 1600 GeV are excluded at 95% confidence level, extending previous limits.

1 Introduction

New strongly interacting particles, if present at the TeV energy scale, may be produced in high-energy proton–proton (pp) collisions and decay to final states with large jet multiplicities. If their decay produces some long-lived particles which interact only weakly, it will also result in a momentum imbalance in the plane transverse to the beam (missing transverse momentum, $\vec{E}_{\mathrm{T}}^{\mathrm{miss}}$ and the magnitude of which is referred to as $E_{\mathrm{T}}^{\mathrm{miss}}$). The decays of new heavy particles may further generate high-mass large-radius hadronic jets, either due to large Lorentz boosts of the massive decay products, or by combinatorial effects in the high-multiplicity events [1].

Such particles are present in supersymmetry (SUSY) [2–7], an extension of the Standard Model (SM) that predicts partner fields for each of the SM particles. These fields combine into physical superpartners of the SM particles. The scalar partners of quarks and leptons are known as squarks ($\tilde{q}$) and sleptons ($\tilde{\ell}$). The fermionic partners of the gluons are the gluinos ($\tilde{g}$), while linear superpositions of the SUSY partners of the Higgs and electroweak gauge bosons form the charginos ($\tilde{\chi}_i^{\pm}$, with i = 1,2) and the neutralinos ($\tilde{\chi}_i^0$ with i = 1,2,3,4), where $\tilde{\chi}_i^{\pm}$ and $\tilde{\chi}_i^0$ are the mass eigenstates, ordered from the lightest to the heaviest.

This note presents the results of a search for new phenomena, such as supersymmetry, in final states with large multiplicities of jets (from ≥8 to ≥10 jets) in association with $E_{\mathrm{T}}^{\mathrm{miss}}$, where those jets are consistent with coming from the decays of heavy objects, and can be clustered into a smaller number of high-mass jets. Such signatures are exhibited, for example, by squark or gluino pair production followed by cascade decay chains, and/or decays to heavy SM particles, such as top quarks or W, Z or Higgs bosons, each of which can produce multiple jets in their decays. In contrast to many other searches for the production of strongly interacting SUSY particles in the hadronic channel at ATLAS [8–14] and CMS [15–25], the requirement made here of large jet multiplicity means that the threshold on $E_{\mathrm{T}}^{\mathrm{miss}}$ can be modest. The dominant standard model backgrounds to this search comprise QCD multijet production and top quark pair-production ($t\bar{t}$) in which the tops decay fully hadronically, or via a tau lepton. By selecting events in which the sum of the masses of the large-radius jets is large, these backgrounds are greatly reduced, increasing sensitivity to decays of heavy objects.

The analysis utilises methods introduced in Ref. [26], and developed from the large-radius jet stream [27] which was used to analyse pp data corresponding to $20.3\,\mathrm{fb}^{-1}$, collected at a centre-of-mass energy $\sqrt{s}$ = 8 TeV. First results with $\sqrt{s}$ = 13 TeV were presented in Ref. [28]. The higher statistics of the present dataset provides increased sensitivity, particularly to particles with larger masses. The online event selection relies on high jet multiplicities and the signal regions (SR) are designed such that the dominant multijet background can be determined from the data using regions of lower $E_{\mathrm{T}}^{\mathrm{miss}}$ and/or lower jet multiplicity, with a selection based on the sum of masses of large-radius reclustered jets, as described in Section 3.

The data were collected by the ATLAS detector [29] in pp collisions at the LHC at a centre-of-mass energy of 13 TeV, during 2015 and until summer 2016. The detector covers the pseudorapidity[1] range of $|\eta| < 4.9$ and is hermetic in azimuth. It consists of an inner tracking detector surrounded by a superconducting solenoid, electromagnetic and hadronic calorimeters, and an external muon spectrometer incorporating large superconducting toroidal magnets. The data were recorded by using a two-level trigger system which

---

[1] ATLAS uses a right-handed coordinate system with its origin at the nominal interaction point (IP) in the centre of the detector and the z-axis along the beam pipe. Cylindrical coordinates (r, ϕ) are used in the transverse plane, ϕ being the azimuthal angle around the beam pipe. The transverse momentum of a four-momentum is $\vec{p}_{\mathrm{T}} = (p_x, p_y)$, its rapidity is $y = \frac{1}{2}\ln\frac{E+p_z}{E-p_z}$, and the pseudorapidity is defined in terms of the polar angle θ as $\eta = -\ln\tan(\theta/2)$.

consists of a hardware-based system followed by a software-based trigger [30]. After applying beam-, data- and detector-quality criteria, the integrated luminosity was $18.2 \pm 0.7\,\mathrm{fb}^{-1}$. The uncertainty was derived using beam-separation scans, following a methodology similar to that detailed in Ref. [31].

2 Physics object definition

Primary vertices are reconstructed using at least two charged particle tracks measured by the inner detector [32]. The primary vertex in the event is defined to be the one with the highest sum of the squared transverse momenta of the tracks forming the vertex ($\sum {p_\mathrm{T}}^2$, where $p_\mathrm{T} = |\vec{p}_\mathrm{T}|$).

Jets are reconstructed using the anti-k_t clustering algorithm [33, 34] with jet radius parameter $R = 0.4$, as implemented in FastJet [35]. The inputs to this algorithm are the energies and positions of clusters of calorimeter cells [36], where the clusters are formed starting from cells with energies significantly above the noise level. The effects of coincident pp interactions ('pileup') on jet energies are accounted for by an event-by-event p_T-density correction [37]. The energy resolution of the jets is improved by using global sequential calibrations [38, 39].

Events with jets originating from cosmic rays, beam background and detector noise are vetoed using the "loose" requirements of Ref. [40, 41]. Jets produced in pileup interactions are rejected using the Jet Vertex Tagger (JVT) [42, 43] multivariate discriminant by discarding all jets with $p_\mathrm{T} < 50$ GeV, $|\eta| < 2.4$ if they have $JVT < 0.59$.

Jets containing b-hadrons (b-jets) are identified using an algorithm exploiting the long lifetime, high decay multiplicity, hard fragmentation and large mass of b-hadrons. The selected working point for the b-tagging algorithm [44, 45] tags b-jets with an efficiency of approximately 70% in simulated $t\bar{t}$ events, and rejects c-jets, τ-jets and light-quark or gluon jets with the rates of 9.6, 31 and 254, respectively. Scale factors measured in data are applied to simulated events selected with b-jets, to improve modelling of the b-tagging (in)efficiencies. All jets are required to satisfy $p_\mathrm{T} > 20$ GeV and $|\eta| < 2.8$. More stringent requirements on p_T and on $|\eta|$ are made when defining signal regions as described in Section 3.

Leptons (electrons and muons) are used to distinguish signal and control regions. "Baseline" lepton candidates are selected, and events containing such leptons are vetoed from the signal regions. Baseline electron candidates are identified by the likelihood-based "Loose" quality criterion described in Ref. [46] using combined track properties in the inner detector and shower shape in calorimeter. Baseline muons are reconstructed with the "Medium" criterion based on combined tracks from the muon spectrometer and the inner detector [47]. Taus are not identified in this analysis. However, the leptons from τ-decays satisfying criteria above are treated as leptons. The baseline electrons and muons are used in the overlap removal process described below.

Photons are not used for event selection, however they are used in the calculation of the missing transverse momentum detailed below. There, they are identified by requiring $p_\mathrm{T} > 25$ GeV and $|\eta| < 2.37$ (excluding $1.37 < |\eta| < 1.52$) and applying the "Tight" selection described in Ref. [48].

To avoid double counting among the reconstructed physics objects, overlap removal was applied in the following procedure. If an electron and a muon candidate share an inner detector track, the electron is removed. Subsequently, leptons are discarded if they fall within $\Delta R_y < 0.4$ of jets that are b-tagged with a fixed b-tag efficiency of 85%, where $\Delta R_y = \sqrt{(\Delta y)^2 + (\Delta\phi)^2}$. Jets that are not b-tagged are removed if they lie within $\Delta R_y < 0.2$ of an electron. If a muon track is ghost-associated [49] to a non-b-tagged jet that has track properties consistent with radiation from the muon, the jet is removed. Finally, if a lepton and any surviving jet have $\Delta R_y < 0.4$, the lepton is removed.

To define the control regions, further selection is applied to the remaining leptons. Electrons and muons are required to have $p_T > 20$ GeV for both and $|\eta| < 2.47$ and 2.5, respectively. Furthermore, electrons are required to satisfy "Tight" quality criterion in Ref. [46]. Signal electrons and muons are required to pass the "GradientLoose" isolation criteria (defined in Ref. [46, 47]). Finally lepton candidates associated to the primary vertex satisfying $|z_0 \sin\theta| < 0.5$mm and $d_0/\sigma(d_0) < 5(3)$ for electrons (muons) where z_0 and d_0 are the longitudinal and transverse impact parameter respectively, are used as signal leptons in this analysis. The efficiency for selecting signal leptons in simulated samples is corrected to match that found in data using scale factors measured in 13 TeV collisions [46, 47].

The missing transverse momentum is defined as the negative vector-sum of momentum of physics objects in the plane perpendicular to beam axis. The reconstruction uses calibrated transverse momenta of all physics objects; jets, electrons, muons and photons, as well as a soft term comprised purely of tracks associated with the primary vertex but not with the other physics objects [50, 51]. The overlap removal in the E_T^{miss} calculation is mainly based on calorimeter cell information, and differs from the procedure used for the selection of analysis objects. To remove events with large E_T^{miss} due to a pileup jet that narrowly passes the JVT selection, a veto is applied to events that contain a jet with $JVT < 0.59, 50 < p_T < 70$ GeV and separated from the E_T^{miss} in azimuth by at least 2.2 radians.

3 Event selection

The signal regions are defined from the jet multiplicity in events with no baseline leptons (e or μ). The jet count, N_{jet}, is defined as the number of jets that satisfy $p_T > 50$ GeV and $|\eta| < 2.0$. The online selection (trigger) for events entering the signal region requires events to have at least six jets with $p_T > 45$ GeV and $|\eta| < 2.4$, and has an efficiency greater than 99.5% for events satisfying the signal selection described below. The same jets that are used in the count are then used as inputs to a second iteration of the anti-k_t clustering algorithm [27, 52], this time using the larger radius of $R = 1.0$. These *reclustered* jets are then used to define the selection variable M_J^Σ, being the sum of the masses of the reclustered jets:

$$M_J^\Sigma = \sum_j m_j^{R=1.0}$$

where the sum is over the masses of all the reclustered jets satisfying $p_T > 100$ GeV and $|\eta| < 1.5$. The signal regions are split into two groups by requiring two different thresholds for the variable M_J^Σ, those being $M_J^\Sigma > 340$ GeV and $M_J^\Sigma > 500$ GeV. Jets with a looser definition than those used in the jet count, requiring $p_T > 40$ GeV and $|\eta| < 2.8$, are used to calculate the scalar sum $H_T = \sum p_T^{\text{jet}}$. The final selection variable is $E_T^{\text{miss}}/\sqrt{H_T}$, the ratio of the E_T^{miss} to the square root of the scalar sum H_T. For all signal regions the threshold on $E_T^{\text{miss}}/\sqrt{H_T}$ is > 4 GeV$^{1/2}$, which gives a good balance between signal acceptance and background rejection. In particular, this cut removes a large portion of the multijet background.

The six signal regions are summarised in Table 1. The signal regions have events in common, for example all of the events in `SR 10j50 MJ340` will also be in the looser `SR 9j50 MJ340`.

Signal region	8j50	9j50	10j50
$R = 0.4$ jet $\|\eta\|$	< 2.0 for all SRs		
$R = 0.4$ jet p_{T}	> 50 GeV for all SRs		
N_{jet}	≥ 8	≥ 9	≥ 10
M_{J}^{Σ}	> 340 GeV or > 500 GeV		
$E_{\mathrm{T}}^{\mathrm{miss}}/\sqrt{H_{\mathrm{T}}}$	$> 4\,\mathrm{GeV}^{1/2}$ for all SRs		

Table 1: Definition of the six signal regions. Selection variable are described in Section 3. Events containing baseline leptons (e or μ) are vetoed.

3.1 Control and validation regions

For each signal region, a number of subsidiary event selections are defined, such that auxiliary measurements can be made to improve the SM background predictions. In all cases, the same M_{J}^{Σ} cut is used as in the signal region, but the jet multiplicity and $E_{\mathrm{T}}^{\mathrm{miss}}/\sqrt{H_{\mathrm{T}}}$ cuts may vary, and additional/alternate criteria on lepton multiplicities and b-tagging may be imposed.

3.1.1 Multijet template and validation regions

The dominant multijet background expectation is determined using a template method, described fully in Section 4.2. Two associated selections are defined: a "template region" selecting exactly six jets and a validation region selecting exactly seven jets (where the jets are the same as those used for the jet count in the signal regions). The full range of $E_{\mathrm{T}}^{\mathrm{miss}}/\sqrt{H_{\mathrm{T}}}$ is used, with low $E_{\mathrm{T}}^{\mathrm{miss}}/\sqrt{H_{\mathrm{T}}}$ bins used for normalisation, whereas the high $E_{\mathrm{T}}^{\mathrm{miss}}/\sqrt{H_{\mathrm{T}}}$ bins allow the extraction and validation of the signal region estimates. Bins of intermediate $E_{\mathrm{T}}^{\mathrm{miss}}/\sqrt{H_{\mathrm{T}}}$ with identical jet multiplicities to the signal regions are used for validation and determination of systematic uncertainties.

3.1.2 Leptonic control regions

Normalisation of the simulated $W \to (\ell\nu)$+jets and semileptonically- or dileptonically-decaying $t\bar{t}$ background components is set by a fit to the data in control regions selecting exactly one electron or muon with a relaxed criterion of $E_{\mathrm{T}}^{\mathrm{miss}}/\sqrt{H_{\mathrm{T}}} > 3\ \mathrm{GeV}^{1/2}$. To increase the event yields, control regions for the N_{jet} signal regions require instead $(N_{\mathrm{jet}} - 1)$ jets. An upper limit of 120 GeV is placed on the transverse mass $m_{\mathrm{T}} = \sqrt{p_{\mathrm{T}}^{\ell} \cdot E_{\mathrm{T}}^{\mathrm{miss}} \left[1 - \cos\left(\Delta\phi_{\ell, E_{\mathrm{T}}^{\mathrm{miss}}}\right)\right]}$ to eliminate contamination from other sources, including potential signals, where p_{T}^{ℓ} is the transverse momentum of the lepton and $\Delta\phi_{\ell, \vec{E}_{\mathrm{T}}^{\mathrm{miss}}}$ is the azimuthal angle between $E_{\mathrm{T}}^{\mathrm{miss}}$ and this lepton.

The largest fraction of the W+jets and $t\bar{t}$ events selected in the signal regions are those in which the W boson decay produces a tau lepton that decays to hadrons, mimicking a quark- or gluon-induced jet. Therefore, to select events in the control regions that more closely resemble those entering the signal regions, the selected electron or muon is treated as a jet for the purposes of jet counting, jet reclustering or H_{T} calculation if its p_{T} and η satisfy the corresponding criteria, as defined above, for jets in the signal region. Separation into W-enriched and $t\bar{t}$-enriched regions is achieved by using b-tags; events with no

b-tags constitute the W-enriched selection, while the requirement of at least one b-tag provides a sample enriched in $t\bar{t}$ events.

4 Background and simulation

Several SM processes contribute to the signal regions. The dominant backgrounds are multijet production (including those from purely strong interaction processes, fully hadronic decays of $t\bar{t}$ and hadronic decays of W and Z bosons in association with jets); semi- and fully-leptonic decays of $t\bar{t}$; and leptonically-decaying W or Z bosons produced in association with jets. Non-fully-hadronic top and W and Z processes are collectively referred to as leptonic backgrounds. They contribute to the signal regions either when no e or μ leptons are produced (for example $Z \rightarrow \nu\nu$ decay or $W \rightarrow \tau\nu$ with hadronically decaying τ), or when leptons are produced but are out of acceptance, are not reconstructed, or are not correctly identified.

The most significant backgrounds (multijet, $t\bar{t}$ and W+jets) are determined with the aid of control regions. These control regions are designed to be kinematically close to the signal regions, enriched in the background process of interest, and free from contamination from the SUSY signal processes under consideration in this search. The multijet background is determined from a data-driven technique, and the leptonic $t\bar{t}$ and W+jets backgrounds use data control regions to normalise the simulation as described in Section 3.1.2. The yields for other, subdominant, leptonic backgrounds are taken from the theoretical calculations described below. These processes include: Z+jets; vector boson pairs (WW, WZ, ZZ); $t\bar{t}$ production in association with W, Z or Higgs bosons; and multi-top production.

Monte Carlo simulations are used in the determination of the leptonic backgrounds and to assess sensitivity to specific SUSY signal models. All simulated events are overlaid with multiple pp collisions simulated with the soft QCD processes of Pythia 8.186 [53] using the A2 set of parameters [54] and the MSTW2008LO parton distribution functions (PDFs) [55]. The simulated events are weighted such that the pileup conditions match those of the data. The response of the detector to particles is modelled with an ATLAS detector simulation [56] based fully on Geant4 [57], or using fast simulation based on a parametrisation of the performance of the ATLAS electromagnetic and hadronic calorimeters [58] and on Geant4 elsewhere. Leptonic background samples use full simulation, while signal samples (described below) use the fast simulation option.

4.1 Leptonic background simulation

For the generation of $t\bar{t}$ and single top-quarks in the Wt and s-channels Powheg-Box v2 [59] was used with the CT10 PDF sets [60] in the matrix element calculations. Electroweak t-channel single top-quark events were generated using Powheg-Box v1. This generator uses the four-flavour scheme for the next-to-leading-order (NLO) matrix element calculations together with the fixed four-flavour PDF set CT10f4 [60]. For this process, the top quarks are decayed using MadSpin [61] preserving all spin correlations, while for all processes the parton shower, fragmentation, and the underlying event are simulated using Pythia v6.428 [62] with the CTEQ6L1 PDF sets [63] and the Perugia 2012 tune (P2012) [64]. The top quark mass is set to 172.5 GeV. The EvtGen v1.2.0 program [65] is used to model properties of the bottom and charm hadron decays for this process and all others not simulated with Sherpa. Simulated $t\bar{t}$ events is normalised to the cross-section calculated to next-to-next-to-leading-order (NNLO) in perturbative QCD, including soft-gluon resummation to next-to-next-to-leading-log (NNLL) order (as described in Ref. [66] and references therein).

Events containing $t\bar{t}$ and additional heavy particles – comprising three-top, four-top, $t\bar{t} + W$, $t\bar{t} + Z$ and $t\bar{t} + WW$ production – are simulated at leading order (LO) in the strong coupling constant α_s, using MadGraph5 v2.2.2 [67] with up to two additional partons in the matrix element, interfaced to the Pythia 8.186 parton shower model. The A14 set of Pythia 8 parameters is used [68], together with the NNPDF2.3 LO PDF set [69]. The predicted production cross-sections are calculated to NLO as described in Ref. [67]. In addition, $t\bar{t} + H$ events are simulated at NLO using MadGraph5_aMC@NLO v2.3.2 [67], with the NNPDF3.0 NLO PDF set [70] used in the matrix element calculation, and again interfaced to Pythia 8.186 for the parton shower, with the A14 tune and the NNPDF2.3 LO PDFs.

Events containing W or Z bosons associated with jets are simulated using the Sherpa 2.2.0 [71] generator. Matrix elements are calculated for up to two partons at NLO and four partons at LO using the Comix [72] and OpenLoops [73] matrix element generators and merged with the Sherpa parton shower [74] using the ME+PS@NLO prescription [75]. The NNPDF3.0 NNLO PDF set is used in association to a tuning performed by the Sherpa authors.

Diboson processes with 4 charged leptons, 3 charged leptons + 1 neutrino, 2 charged leptons and 2 neutrinos, are simulated using Sherpa v2.1.1 [71]. The matrix element calculations contain all diagrams with four electroweak vertices. They are calculated for up to one (for 4ℓ, $2\ell{+}2\nu$) or without additional partons (for $3\ell{+}1\nu$) at NLO and up to three additional partons at LO using the Comix and OpenLoops matrix element generators and merged with the Sherpa parton shower using the ME+PS@NLO prescription. The CT10 PDF set is used in conjunction with dedicated parton shower tuning developed by the Sherpa authors. An identical procedure is followed to simulate diboson production with one hadronic boson decay accompanied by 1 charged lepton and 1 neutrino, 2 charged leptons or 2 neutrinos, where the calculations include one additional parton at NLO for $ZZ \rightarrow 2\ell + q\bar{q}$ and $ZZ \rightarrow 2\nu + q\bar{q}$ only, and up to three additional partons at LO.

Theoretical uncertainties are considered on all these simulated samples. By far the most important process simulated in this analysis is $t\bar{t}$, and to evaluate the uncertainty on this background several samples are compared. Samples are produced with the factorisation and renormalisation scales varied coherently, along with variations of the h_{damp} parameter and with more/less radiation tunes of the parton shower [76]. Additionally to account for uncertainties in the parton shower modelling and generator choice, the nominal sample is compared to samples generated with Powheg-Box and MadGraph5_aMC@NLO, interfaced to Herwig++ [77], and to MadGraph5 samples generated at LO with up to two additional partons in the matrix element. The comparison with samples which vary the amount of additional radiation contributes the largest uncertainty on the signal region predictions.

Further details of samples can be found in Refs. [76, 78–81].

4.2 Multijet background

The dominant background in the signal regions is from the multijet processes described above. Events with large jet multiplicities, such as those under study in this analysis, cannot be accurately modelled by MC simulations and therefore a data-driven technique is employed. This method relies on the observation [26] that the $E_{\mathrm{T}}^{\mathrm{miss}}$ resolution of the detector is approximately proportional to $\sqrt{H_{\mathrm{T}}}$ and almost independent of the jet multiplicity for events when the $E_{\mathrm{T}}^{\mathrm{miss}}$ predominately originates from calorimeter energy mismeasurement.

This being the case, it is possible to use the lower multiplicity template regions as defined in Section 3 to measure the $E_{\mathrm{T}}^{\mathrm{miss}}/\sqrt{H_{\mathrm{T}}}$ shape in data. The approximate invariance of this shape as the jet multiplicity increases therefore permits a prediction of the multijet yield in the signal region, provided the template is normalised to the data at low $E_{\mathrm{T}}^{\mathrm{miss}}/\sqrt{H_{\mathrm{T}}}$.

In practice, the increasing fraction of W+jets and more so $t\bar{t}$ events at large $E_{\mathrm{T}}^{\mathrm{miss}}/\sqrt{H_{\mathrm{T}}}$ necessitates an MC-based background subtraction in the extraction of the $E_{\mathrm{T}}^{\mathrm{miss}}/\sqrt{H_{\mathrm{T}}}$ template. This is further modified by fits to the leptonic control regions, described later in Section 6. The template extracted from the 6-jet control region is then simply added to the MC-based estimates of other background components, with the normalisation being determined by the N_{jet} yields in the region with $E_{\mathrm{T}}^{\mathrm{miss}}/\sqrt{H_{\mathrm{T}}} < 1.5\,\mathrm{GeV}^{1/2}$, where the purity of multijet events is very high.

Unlike in previous analyses [27, 28], no minimum H_{T} cut has been required, as the high thresholds on M_{J}^{Σ} imply already that the $E_{\mathrm{T}}^{\mathrm{miss}}$ measurement is dominated by jet contributions. Therefore, so is the $E_{\mathrm{T}}^{\mathrm{miss}}$ resolution. Systematic uncertainties on the multijet template estimate are derived as described in Section 5.

4.3 SUSY signal models

Two classes of SUSY signal model are used when interpreting the results. The first is a simplified model, in which gluinos are pair-produced and then decay via the cascade

$$\begin{aligned}
\tilde{g} &\rightarrow q + \bar{q}' + \tilde{\chi}_1^{\pm} \quad (q = u, d, s, c) \\
\tilde{\chi}_1^{\pm} &\rightarrow W^{\pm} + \tilde{\chi}_2^0 \\
\tilde{\chi}_2^0 &\rightarrow Z + \tilde{\chi}_1^0.
\end{aligned}$$

The parameters of the model are the masses of the gluino, $m_{\tilde{g}}$, and the lightest neutralino, $m_{\tilde{\chi}_1^0}$. The mass of the $\tilde{\chi}_1^{\pm}$ is constrained to be $\frac{1}{2}(m_{\tilde{g}} + m_{\tilde{\chi}_1^0})$ and the mass of the $\tilde{\chi}_2^0$ to be $\frac{1}{2}(m_{\tilde{\chi}_1^{\pm}} + m_{\tilde{\chi}_1^0})$. This model is labelled in the following figures as ‘2-step’.

The second type of SUSY model is drawn from a two-dimensional subspace (a ‘slice’) of the 19-parameter phenomenological minimal supersymmetric Standard Model (pMSSM) [82, 83]. The selection is motivated in part by models not previously excluded in the analysis of Ref. [84]. The models are selected to have a bino-like $\tilde{\chi}_1^0$, kinematically accessible gluinos, and a Higgsino-like multiplet at intermediate mass. The Higgsino multiplet contains two neutralinos (the $\tilde{\chi}_2^0$ and $\tilde{\chi}_3^0$) and a chargino (the $\tilde{\chi}_1^{\pm}$). The mass of these particles is varied by changing the SUSY soft-breaking parameters M_3 (for the gluino) and μ (for the Higgsinos), while , M_1 (for the $\tilde{\chi}_1^0$) is held constant at 60 GeV. In order that other SUSY particles remain kinematically inaccessible, the other parameters, defined in Ref. [84], are set to $m_A = M_2 = 3$ TeV, $A_\tau = 0$, $\tan\beta = 10$, $A_t = A_b = m_{(\tilde{e},\tilde{\mu},\tilde{\tau})L} = m_{(\tilde{e},\tilde{\mu},\tilde{\tau})R} = m_{\tilde{q}L(1,2,3)} = m_{(\tilde{u},\tilde{c},\tilde{t})R} = m_{(\tilde{d},\tilde{s},\tilde{b})R} = 5$ TeV. Mass spectra with consistent electroweak symmetry breaking are generated using SOFTSUSY 3.4.0 [85]. The decay branching ratios are calculated with SDECAY/HDECAY 1.3b/3.4 [86], and when $m_{\tilde{\chi}_1^{\pm}} \lesssim 500$ GeV and $m_{\tilde{g}} \gtrsim 1200$ GeV the predominant decays are $\tilde{g} \rightarrow t + \bar{t} + \tilde{\chi}_{2,3}^0$ and $\tilde{g} \rightarrow t + \bar{b} + \tilde{\chi}_1^{\pm}$, with $\tilde{\chi}_{2,3}^0$ decaying to $Z/h + \tilde{\chi}_1^0$ and $\tilde{\chi}_1^{\pm}$ to $W^{\pm} + \tilde{\chi}_1^0$. When these decays dominate they lead to final states with many jets, but relatively little $E_{\mathrm{T}}^{\mathrm{miss}}$. This renders this search particularly sensitive over most other SUSY searches which tend to require high $E_{\mathrm{T}}^{\mathrm{miss}}$. At higher $m_{\tilde{\chi}_1^\pm}$ and lower $m_{\tilde{g}}$, the decay $\tilde{g} \rightarrow qq\tilde{\chi}_1^0$ becomes dominant and this search starts to lose sensitivity. This model is labelled in the following figures as 'pMSSM'.

The signal events are simulated using MadGraph5 v2.2.2 at LO interfaced to Pythia 8.186. The A14 tune parameters are used, together with the NNPDF2.3 LO PDF set. The EvtGen v1.2.0 program is used for properties of the bottom and charm hadron decays. The signal cross-sections are calculated at NLO in the strong coupling constant, adding the resummation of soft gluon emission at next-to-leading-logarithmic accuracy (NLO+NLL) [87–91]. The nominal cross-section is taken from an envelope of cross-section predictions using different PDF sets and factorisation and renormalisation scales, as described in Ref. [92].

For an example 2-step model point with $m_{\tilde{g}} = 1400$ GeV and $m_{\tilde{\chi}_1^0} = 200$ GeV, the SR selection efficiencies range from 7-26%, while for a similar pMSSM model point with $m_{\tilde{g}} = 1400$ GeV and $m_{\tilde{\chi}_1^\pm} = 200$ GeV, the selection efficiencies are 5.5-17%.

5 Systematic uncertainties

Systematic uncertainties in this analysis arise from a number of sources. Predictions of the signal and background using MC simulation are affected by experimental systematics on the energy scales and resolutions for jets and leptons, as well as on efficiencies for particle identification and reconstruction. Theoretical uncertainties on the overall and differential cross-sections for simulated SM processes likewise lead to uncertainties in the SM background yields. Sources of variation in the data-driven multijet template shape are also assessed as sources of systematic uncertainties.

5.1 Experimental systematics

Uncertainties on the scale and resolution of the energy/momentum measurements of jets, leptons and $E_{\mathrm{T}}^{\mathrm{miss}}$ are assessed by applying scale offsets or smearing to the simulated object kinematics. In the signal regions, the dominant uncertainties are those on the jet energy scale [39, 93, 94] and resolution [95, 96], which typically result in 15% variations in the yields.

The luminosity uncertainty [31] affects signal yields as well as MC-based background predictions whose normalisations are not fixed by data. A pileup uncertainty is applied to all MC, covering potential mismodelling in the amount of pileup activity overlaid on the hard scatter events.

5.2 Theoretical systematics

Modelling uncertainties on the production of $t\bar{t}$ are assessed using MC samples varying the parton shower and matrix element generators, as well as the amount of additional radiation, as described in Section 4.1. Similarly, uncertainties on W+jets production are quantified by varying the factorisation, renormalisation, resummation and jet matching scales in Sherpa. The largest uncertainty on the signal region predictions arises from the comparison with the $t\bar{t}$ samples varying the amount of additional radiation, which can be in excess of 70%.

The remaining simulated background components are assigned conservative overall normalisation uncertainties as follows: 30% on single top and $t\bar{t}$ in association with bosons or multi-top production; 40% on

Z+jets; and 50% on diboson production. Due to the small contributions of these processes to the signal region background expectations, these uncertainties are by far subdominant to the $t\bar{t}$ theory systematics and uncertainties on the multijet estimate.

5.3 Multijet template systematics

Uncertainties on the data-driven prediction of the multijet background are extracted from closure tests of the method, defined as the largest disagreement observed between data and prediction in validation regions with $N_{\text{jets}} = 7$ and/or $E_{\text{T}}^{\text{miss}}/\sqrt{H_{\text{T}}} < 4\,\text{GeV}^{1/2}$. These amount to 7-8% in the 8-jet signal regions and 13-16% in the 9- and 10-jet signal regions.

Further systematic uncertainties are applied to cover possible variations in the template prediction due to differences in the flavour composition and overall jet activity between the signal and control regions. A comparison between the nominal template estimate and a prediction derived as the sum of two templates (this prediction is constructed as a weighted sum of the nominal with a template using exactly 0 or at least 1 b-tagged jet) produces an uncertainty of 8.3%, which is the largest systematic measured from the different validation regions. Finally, a 5% uncertainty is added to cover deviations in the template estimate due to kinematic differences between the control and signal regions.

6 Statistical methods

A self-consistent background estimate, allowing the normalisation of the MC-driven background components to be corrected to measurements in data, is extracted for each signal region using a simultaneous fit to the corresponding leptonic control regions and 6-jet template region. This background fit is carried out using the HistFitter package [97]. The fit is extended to include constraints from the signal region in two configurations, allowing hypothesis tests in the contexts of exclusion and discovery. These hypothesis tests use log-likelihood ratio test statistics as defined in Ref. [98].

6.1 Background fit

To perform the background fit two leptonic control regions, as defined in Section 3, are used to fix the normalisation of the $t\bar{t}$ and W+jets processes. For each background process constrained by the fit, an unconstrained normalisation factor μ_b, $b \in \{t\bar{t}, W\}$ is defined, such that $\mu_b = 1$ implies consistency with the nominal MC cross-section. A likelihood is then constructed for the ensemble of measurements in the control regions as the product of Poisson distributions whose means are specified by the nominal MC estimate for that region, including the free normalisation factors μ_b. The systematic uncertainties described in Section 5 are implemented in the form of gaussian-constrained nuisance parameters modifying the Poisson mean of each background component contributing to the estimate in a given signal or control region.

Minimisation of the likelihood (profiling) fixes the values of, and uncertainties on, μ_b, which can then be combined with the MC and template predictions to obtain the total background prediction in the signal region.

6.2 Discovery fit

To quantify the significance of any potential excess in the signal region, the likelihood function defined above is augmented with a measurement in the signal region, while all signal and control regions are assumed to remain free of signal. A frequentist hypothesis test is carried out, determining the discovery p-value p_0.

6.3 Exclusion fit

To set exclusion limits on particular signal models, the signal region is added to the background fit, as in the discovery case, but now a signal yield n_s and signal strength parameter μ_s are included in addition to the background expectations in all signal and control regions. Signal contamination in the control regions is thereby accounted for.

The exclusion p-value p_1 is determined from a hypothesis test, and the CL_s convention [99] is followed, in which p_1 is divided by the background p-value CL_b, limiting the enhancement of exclusion limits due to downward fluctuations in the data. A given signal model is excluded at the 95% confidence level if the one-sided gaussian significance $Z_1(CL_s) > 1.64$.

To obtain signal model independent exclusion limits for each signal region, the hypothesis test is repeated in a scan over signal yields, assuming that the corresponding control regions are free of contamination, until the yield corresponding to 95% CL_s exclusion significance is determined. This establishes the upper limit set by that signal region on the visible signal cross-section $\epsilon\sigma$, i.e. the product of the cross-section and selection efficiency.

7 Results

Signal region	Fitted background			Observed events
	Multijet	Leptonic	Total	
`SR 8j50 MJ340`	312 ± 29	155 ± 30	467 ± 40	424
`SR 9j50 MJ340`	73 ± 10	38 ± 14	110 ± 16	99
`SR 10j50 MJ340`	14.1 ± 2.1	9.3 ± 5.9	23.4 ± 6.1	22
`SR 8j50 MJ500`	107.4 ± 8.7	46 ± 16	153 ± 17	141
`SR 9j50 MJ500`	33.4 ± 5.6	14 ± 10	48 ± 11	48
`SR 10j50 MJ500`	8.6 ± 1.6	4.0 ± 4.1	12.5 ± 4.2	15

Table 2: The expected SM background (and separately the multijet and leptonic contributions) and the observed number of data events for each of the six signal regions. The SM background normalisations are obtained from the background fit, as described in Section 6.1. The signal regions are as defined in Table 1.

Figure 1 shows the post-fit $E_{\mathrm{T}}^{\mathrm{miss}}/\sqrt{H_{\mathrm{T}}}$ distributions in the signal regions. The yields in each of the 6 signal regions are reported in Table 2, and summarised in Figure 2. No significant excess is observed above the SM expectations in any signal region, and all observed event counts are consistent with the background-only expectation. Table 3 shows the model-independent limits – 95% confidence level (CL)

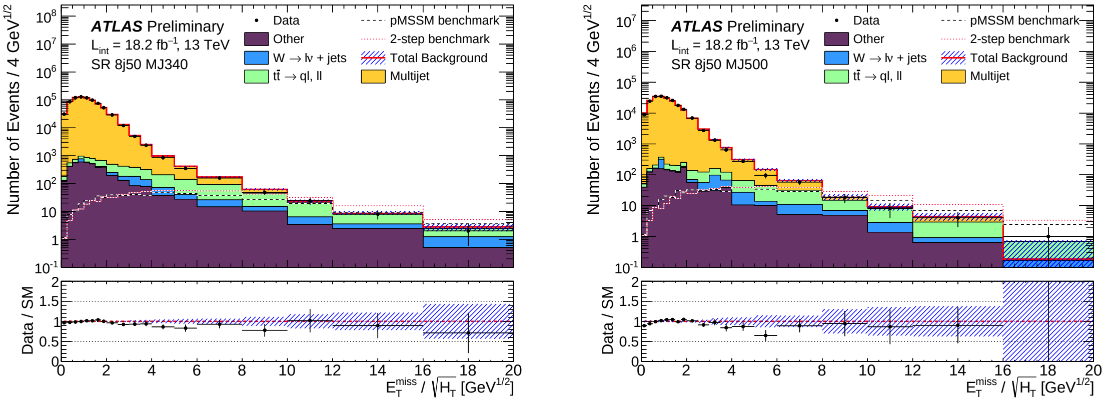

(a) $N_{\text{jet}} \geq 8,\ M_J^{\Sigma} > 340$ GeV (b) $N_{\text{jet}} \geq 8,\ M_J^{\Sigma} > 500$ GeV

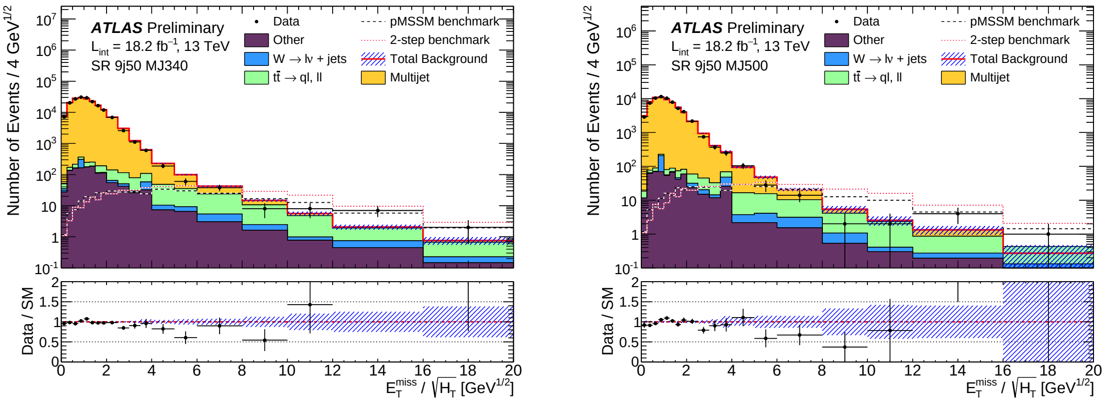

(c) $N_{\text{jet}} \geq 9,\ M_J^{\Sigma} > 340$ GeV (d) $N_{\text{jet}} \geq 9,\ M_J^{\Sigma} > 500$ GeV

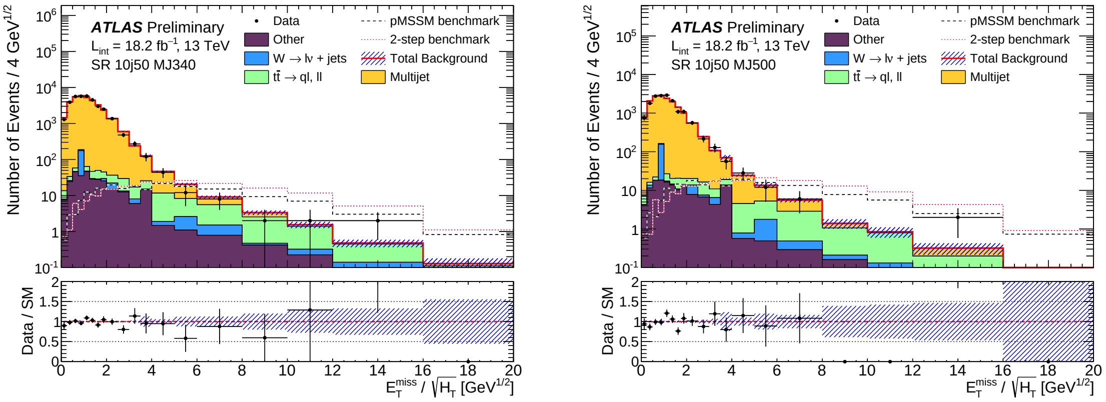

(e) $N_{\text{jet}} \geq 10,\ M_J^{\Sigma} > 340$ GeV (f) $N_{\text{jet}} \geq 10,\ M_J^{\Sigma} > 500$ GeV

Figure 1: Distributions of the selection variable $E_T^{\text{miss}}/\sqrt{H_T}$ for events with at least 8, 9 and 10 jets. All signal region selections have been applied other than those on $E_T^{\text{miss}}/\sqrt{H_T}$ itself. The plots on the left require $M_J^{\Sigma} > 340$ GeV, while those on the right require $M_J^{\Sigma} > 500$ GeV. The leptonic backgrounds are normalised to their post-fit values. The dashed lines indicate the prediction for several different simplified model scenarios for different gluino and $\tilde{\chi}_1^0$ masses. The sub-plots show the ratio of the data to the SM prediction. The blue hatched band shows the statistical uncertainty arising from a finite number of MC events and limited data in the templates and $E_T^{\text{miss}}/\sqrt{H_T} < 1.5$ normalisation regions. The dashed lines labelled 'pMSSM'and '2-Step' refer to benchmark signal points – a pMSSM slice model with $(m(\tilde{g}), m(\tilde{\chi}_1^{\pm})) = (1400, 200)$ GeVand a cascade decay model with $(m(\tilde{g}), m(\tilde{\chi}_1^0)) = (1400, 200)$ GeV.

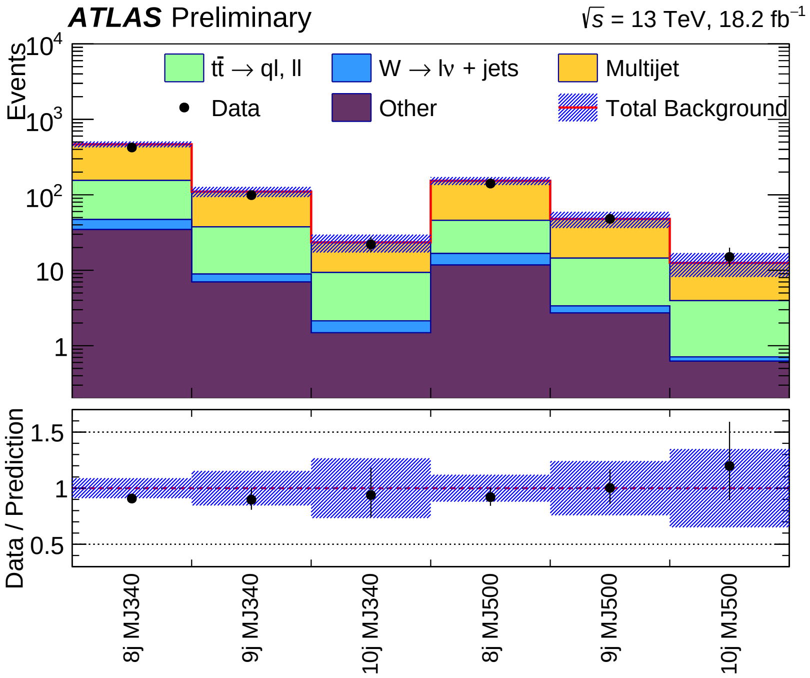

Figure 2: Summary plot showing the data and SM predictions for the six signal regions. The sub-plot shows the ratio of the yields to the SM predictions. The blue band shows the combined statistical and systematic uncertainty on the predictions after the background fit described in Section 6.1.

Signal channel	$\langle\epsilon\sigma\rangle_{\mathrm{obs}}^{95}$[fb]	S_{obs}^{95}	S_{exp}^{95}
`SR 8j50 MJ340`	3.5	64	82^{+20}_{-20}
`SR 9j50 MJ340`	1.7	32	35^{+14}_{-4}
`SR 10j50 MJ340`	1.1	19	19^{+1}_{-0}
`SR 8j50 MJ500`	1.9	34	41^{+13}_{-8}
`SR 9j50 MJ500`	1.6	29	27^{+8}_{-6}
`SR 10j50 MJ500`	0.83	15	12^{+4}_{-2}

Table 3: Results from the exclusion fit, described in Section 6.2. Left to right: 95% CL upper limits on the visible cross section ($\langle\epsilon\sigma\rangle_{\mathrm{obs}}^{95}$) and on the number of signal events (S_{obs}^{95}). The third column (S_{exp}^{95}) shows the 95% CL upper limit on the number of signal events, given the expected number (and $\pm 1\sigma$ excursions on the expectation) of background events.

limits on the maximum contribution of new physics processes to the event yields in the various SRs, assuming zero signal contamination in control regions.

The results are interpreted in the context of the two supersymmetric models described in Section 4.3. The 95% CL exclusion limits on these models are obtained for each signal region as described in Section 6.3. All uncertainties on the SM expectation are considered, including those which are correlated between signal and background (for instance jet energy scale uncertainties) and likewise all uncertainties on the signal expectation are included, except theoretical cross-section uncertainties (PDF and scale), which are indicated explicitly as separate contours.

The resulting exclusion regions are shown in Figure 3. For each signal model point, the signal region with the best expected limit is used. The sensitivity of the respective signal regions varies with the model parameters, with the looser signal regions contributing at lower gluino masses and higher chargino/neutralino masses in the pMSSM/simplified model planes respectively, while the strongest limits at large gluino masses are set by `SR 10j50 MJ500`. For the pMSSM slice, gluino masses up to 1550 GeV are excluded at the 95% CL, while for the simplifed model, gluino masses up to 1600 GeV are excluded. In both cases these results significantly extend previous bounds.

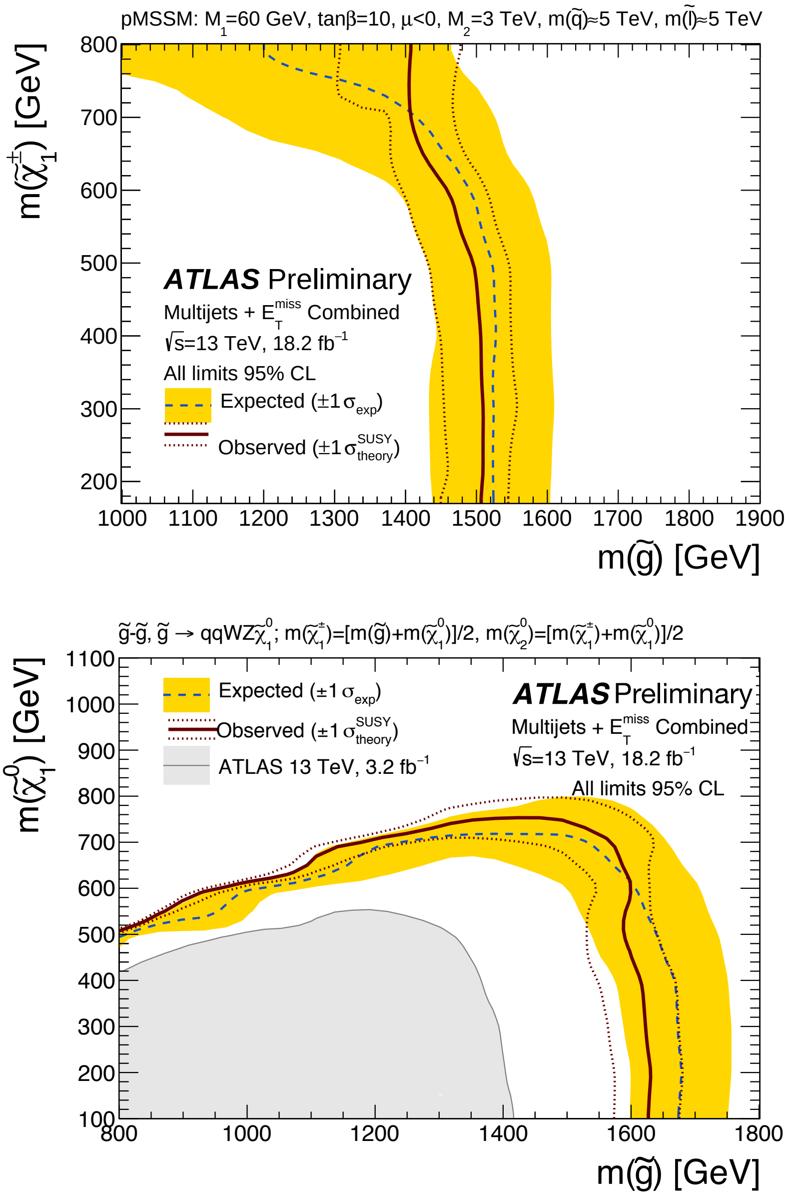

Figure 3: The 95% CL exclusion curves for the two supersymmetric models described in the text. The solid red and dashed blue curves show the 95% CL observed and expected limits, respectively, including all uncertainties except the theoretical signal cross-section uncertainty (PDF and scale). The dotted red lines bracketing the observed limit represent the result produced when moving the signal cross-section by $\pm1\sigma$ (as defined by the PDF and scale uncertainties). The shaded yellow band around the expected limit shows the $\pm1\sigma$ variation of the expected limit. The shaded grey area shows the observed exclusion from a previous ATLAS analysis [28]. Excluded regions are below and to the left of the relevant lines.

8 Conclusion

A search is presented for new phenomena with large jet multiplicities (from ≥ 8 to ≥ 10) and missing transverse momentum, where the jets are consistent with coming from the decays of heavy objects, and so can be clustered into a smaller number of high-mass jets. The search uses $18.2\,\mathrm{fb}^{-1}$ of $\sqrt{s} = 13$ TeV pp collision data collected by the ATLAS experiment at the Large Hadron Collider. The increase in the LHC centre-of-mass energy provides increased sensitivity to higher-mass sparticles. The sensitivity to new physics is enhanced by considering the scalar sum of masses of radius $R = 1.0$ jets in the event, reconstructed using the anti-k_t clustering algorithm. The Standard Model predictions are found to be consistent with the data. The results are interpreted in the context of a simplified supersymmetry model, and a slice of the pMSSM, each of which predict cascade decays of supersymmetric particles and hence large jet multiplicities. The data exclude gluino masses up to 1600 GeV at the 95% CL, extending previous bounds. Model-independent limits are presented which allow reinterpretation of the results to cases of other models which also predict decays into multijet final states in association with invisible particles.

References

[1] T. Cohen et al., *Jet Substructure by Accident*, JHEP **03** (2013) 161, arXiv: `1212.1456 [hep-ph]`.

[2] Y. A. Golfand and E. P. Likhtman, *Extension of the Algebra of Poincare Group Generators and Violation of p Invariance*, JETP Lett. **13** (1971) 323, [Pisma Zh.Eksp.Teor.Fiz.13:452-455,1971].

[3] D. V. Volkov and V. P. Akulov, *Is the Neutrino a Goldstone Particle?*, Phys. Lett. **B 46** (1973) 109.

[4] J. Wess and B. Zumino, *Supergauge Transformations in Four-Dimensions*, Nucl. Phys. **B 70** (1974) 39.

[5] J. Wess and B. Zumino, *Supergauge Invariant Extension of Quantum Electrodynamics*, Nucl. Phys. **B 78** (1974) 1.

[6] S. Ferrara and B. Zumino, *Supergauge Invariant Yang-Mills Theories*, Nucl. Phys. **B 79** (1974) 413.

[7] A. Salam and J. A. Strathdee, *Supersymmetry and Nonabelian Gauges*, Phys. Lett. **B 51** (1974) 353.

[8] ATLAS Collaboration, *Search for squarks and gluinos using final states with jets and missing transverse momentum with the ATLAS detector in* $\sqrt{s} = 7$ *TeV proton–proton collisions*, Phys. Lett. B **701** (2011) 186, arXiv: `1102.5290 [hep-ex]`.

[9] ATLAS Collaboration, *Search for squarks and gluinos using final states with jets and missing transverse momentum with the ATLAS detector in* $\sqrt{s} = 7$ *TeV proton–proton collisions*, Phys. Lett. B **710** (2012) 67, arXiv: `1109.6572 [hep-ex]`.

[10] ATLAS Collaboration, *Search for squarks and gluinos with the ATLAS detector in final states with jets and missing transverse momentum using* $4.7\ fb^{-1}$ *of* $\sqrt{s} = 7$ *TeV proton–proton collision data*, Phys. Rev. D **87** (2013) 012008, arXiv: `1208.0949 [hep-ex]`.

[11] ATLAS Collaboration, *Search for squarks and gluinos with the ATLAS detector in final states with jets and missing transverse momentum using* $\sqrt{s} = 8$ *TeV proton–proton collision data*, JHEP **09** (2014) 176, arXiv: `1405.7875 [hep-ex]`.

[12] ATLAS Collaboration, *Summary of the searches for squarks and gluinos using* $\sqrt{s} = 8$ *TeV pp collisions with the ATLAS experiment at the LHC*, JHEP **10** (2015) 054, arXiv: `1507.05525 [hep-ex]`.

[13] ATLAS Collaboration, *Search for squarks and gluinos in final states with jets and missing transverse momentum at* $\sqrt{s}$ *= 13 TeV with the ATLAS detector*, Eur. Phys. J. **C76** (2016) 392, arXiv: `1605.03814 [hep-ex]`.

[14] ATLAS Collaboration, *Further searches for squarks and gluinos in final states with jets and missing transverse momentum at* $\sqrt{s}$ *=13 TeV with the ATLAS detector*, ATLAS-CONF-2016-078, 2016, URL: `https://cds.cern.ch/record/2206252`.

[15] CMS Collaboration, *Search for supersymmetry in hadronic final states with missing transverse energy using the variables* α_T *and b-quark multiplicity in pp collisions at 8 TeV*, Eur. Phys. J. C **73** (2013) 2568, arXiv: `1303.2985 [hep-ex]`.

[16] CMS Collaboration, *Inclusive search for supersymmetry using the razor variables in pp collisions at* $\sqrt{s} = 7$ *TeV*, Phys. Rev. Lett. **111** (2013) 081802, arXiv: `1212.6961 [hep-ex]`.

[17] CMS Collaboration,
Search for supersymmetry in hadronic final states using MT2 in pp collisions at $\sqrt{s} = 7$ *TeV*,
JHEP **10** (2012) 018, arXiv: `1207.1798 [hep-ex]`.

[18] CMS Collaboration, *Search for new physics in the multijet and missing transverse momentum final state in proton-proton collisions at* $\sqrt{s} = 7$ *TeV*, Phys. Rev. Lett. **109** (2012) 171803,
arXiv: `1207.1898 [hep-ex]`.

[19] CMS Collaboration,
Search for Supersymmetry at the LHC in Events with Jets and Missing Transverse Energy,
Phys. Rev. Lett. **107** (2011) 221804, arXiv: `1109.2352 [hep-ex]`.

[20] CMS Collaboration, *Searches for Supersymmetry using the* M_{T2} *Variable in Hadronic Events Produced in pp Collisions at 8 TeV*, JHEP **05** (2015) 078, arXiv: `1502.04358 [hep-ex]`.

[21] CMS Collaboration, *Search for new physics in the multijet and missing transverse momentum final state in proton-proton collisions at* $\sqrt{s}$*= 8 TeV*, JHEP **06** (2014) 055,
arXiv: `1402.4770 [hep-ex]`.

[22] CMS Collaboration, *Search for supersymmetry in hadronic final states with missing transverse energy using the variables* α_T *and b-quark multiplicity in pp collisions at* $\sqrt{s} = 8$ *TeV*,
Eur. Phys. J. C **73** (2013) 2568, arXiv: `1303.2985 [hep-ex]`.

[23] CMS Collaboration, *Search for new physics in final states with jets and missing transverse momentum in* $\sqrt{s}$ *= 13 TeV pp collisions with the* α_T *variable*, CMS-PAS-SUS-15-005 (2015),
URL: `http://inspirehep.net/record/1410157`.

[24] CMS Collaboration,
Inclusive search for supersymmetry using the razor variables at sqrt(s) = 13 TeV,
CMS-PAS-SUS-15-004 (2015), URL: `https://cds.cern.ch/record/2114815`.

[25] CMS Collaboration, *Search for new physics with the MT2 variable in all-jets final states produced in pp collisions at sqrt(s) = 13 TeV*, Submitted to JHEP (2016), arXiv: `1603.04053 [hep-ex]`.

[26] ATLAS Collaboration, *Search for new phenomena in final states with large jet multiplicities and missing transverse momentum using* $\sqrt{s} = 7$ *TeV pp collisions with the ATLAS detector*,
JHEP **11** (2011) 099, arXiv: `1110.2299 [hep-ex]`.

[27] ATLAS Collaboration,
Search for new phenomena in final states with large jet multiplicities and missing transverse momentum at $\sqrt{s} = 8$ *TeV proton–proton collisions using the ATLAS experiment*,
JHEP **10** (2013) 130, arXiv: `1308.1841 [hep-ex]`.

[28] ATLAS Collaboration, *Search for new phenomena in final states with large jet multiplicities and missing transverse momentum with ATLAS using* $\sqrt{s} = 13$ *TeV proton–proton collisions*,
Phys. Lett. B **757** (2016) 334, arXiv: `1602.06194 [hep-ex]`.

[29] ATLAS Collaboration, *The ATLAS Experiment at the CERN Large Hadron Collider*,
JINST **3** (2008) S08003.

[30] ATLAS Collaboration, *2015 start-up trigger menu and initial performance assessment of the ATLAS trigger using Run-2 data*, ATL-DAQ-PUB-2016-001, 2016,
URL: `https://cds.cern.ch/record/2136007`.

[31] ATLAS Collaboration, *Improved luminosity determination in pp collisions at* $\sqrt{s} = 7$ *TeV using the ATLAS detector at the LHC*, Eur. Phys. J. C **73** (2013) 2518, arXiv: `1302.4393 [hep-ex]`.

[32] ATLAS Collaboration,
Vertex Reconstruction Performance of the ATLAS Detector at $\sqrt{s}$ = 13 *TeV*,
ATL-PHYS-PUB-2015-026, 2016, URL: http://cds.cern.ch/record/2037717.

[33] M. Cacciari, G. P. Salam and G. Soyez, *The Anti-k(t) jet clustering algorithm*,
JHEP **04** (2008) 063, arXiv: 0802.1189 [hep-ph].

[34] M. Cacciari and G. P. Salam, *Dispelling the* N^3 *myth for the* k_t *jet-finder*,
Phys. Lett. **B 641** (2006) 57, arXiv: hep-ph/0512210.

[35] M. Cacciari, G. P. Salam and G. Soyez, *FastJet user manual*, (2011),
arXiv: 1111.6097 [hep-ph], URL: http://fastjet.fr/.

[36] ATLAS Collaboration,
Topological cell clustering in the ATLAS calorimeters and its performance in LHC Run 1, (2016),
arXiv: 1603.02934 [hep-ex].

[37] ATLAS Collaboration, *Performance of pile-up mitigation techniques for jets in pp collisions at* $\sqrt{s}$ = 8 *TeV using the ATLAS detector*, (2015), arXiv: 1510.03823 [hep-ex].

[38] ATLAS Collaboration, *Jet global sequential corrections with the ATLAS detector in proton–proton collisions at* $\sqrt{s}$ = 8 *TeV*, ATLAS-CONF-2015-002, 2015,
URL: http://cdsweb.cern.ch/record/2001682.

[39] ATLAS Collaboration, *Jet Calibration and Systematic Uncertainties for Jets Reconstructed in the ATLAS Detector at* $\sqrt{s}$ = 13 *TeV*, ATL-PHYS-PUB-2015-015, 2015,
URL: https://cds.cern.ch/record/2037613.

[40] ATLAS Collaboration, *Characterisation and mitigation of beam-induced backgrounds observed in the ATLAS detector during the 2011 proton–proton run*, JINST **8** (2013) P07004,
arXiv: 1303.0223 [hep-ex].

[41] ATLAS Collaboration,
Selection of jets produced in 13 *TeV proton–proton collisions with the ATLAS detector*,
ATLAS-CONF-2015-029, 2015, URL: http://cdsweb.cern.ch/record/2037702.

[42] ATLAS Collaboration, *Tagging and suppression of pileup jets with the ATLAS detector*,
ATLAS-CONF-2014-018, 2014, URL: http://cdsweb.cern.ch/record/1700870.

[43] ATLAS Collaboration,
Performance of pile-up mitigation techniques for jets in pp collisions with the ATLAS detector,
Nucl. Instrum. Meth. **A824** (2016) 367, arXiv: 1510.03823 [hep-ex].

[44] ATLAS Collaboration, *Performance of b-Jet Identification in the ATLAS Experiment*,
JINST **11** (2016) P04008, arXiv: 1512.01094 [hep-ex].

[45] ATLAS Collaboration, *Optimisation of the ATLAS b-tagging performance for the 2016 LHC Run*,
ATL-PHYS-PUB-2016-012, 2016, URL: https://cds.cern.ch/record/2160731.

[46] ATLAS Collaboration, *Electron efficiency measurements with the ATLAS detector using the 2015 LHC proton-proton collision data*, ATLAS-CONF-2016-024, 2016,
URL: http://cds.cern.ch/record/2157687.

[47] ATLAS Collaboration, *Muon reconstruction performance of the ATLAS detector in proton–proton collision data at* $\sqrt{s}$ = 13 *TeV*, (2016), arXiv: 1603.05598 [hep-ex].

[48] ATLAS Collaboration, *Measurement of the photon identification efficiencies with the ATLAS detector using LHC Run-1 data*, (2016), arXiv: 1606.01813 [hep-ex].

[49] M. Cacciari, G. P. Salam and G. Soyez, *The Catchment Area of Jets*, JHEP **04** (2008) 005, arXiv: `0802.1188 [hep-ph]`.

[50] ATLAS Collaboration, *Expected performance of missing transverse momentum reconstruction for the ATLAS detector at* $\sqrt{s} = 13$ *TeV*, ATL-PHYS-PUB-2015-023, 2015, URL: `http://cds.cern.ch/record/2037700`.

[51] ATLAS Collaboration, *Performance of missing transverse momentum reconstruction for the ATLAS detector in the first proton-proton collisions at at* $\sqrt{s}$*= 13 TeV*, ATL-PHYS-PUB-2015-027, 2015, URL: `http://cds.cern.ch/record/2037904`.

[52] B. Nachman et al., *Jets from Jets: Re-clustering as a tool for large radius jet reconstruction and grooming at the LHC*, JHEP **02** (2015) 075, arXiv: `1407.2922 [hep-ph]`.

[53] T. Sjöstrand, S. Mrenna and P. Z. Skands, *A Brief Introduction to PYTHIA 8.1*, Comput. Phys. Commun. **178** (2008) 852, arXiv: `0710.3820 [hep-ph]`.

[54] ATLAS Collaboration, *Summary of ATLAS Pythia 8 tunes*, ATL-PHYS-PUB-2012-003, 2012, URL: `https://cds.cern.ch/record/1474107`.

[55] A. D. Martin, W. J. Stirling, R. S. Thorne and G. Watt, *Parton distributions for the LHC*, Eur. Phys. J. **C 63** (2009) 189, arXiv: `0901.0002 [hep-ph]`.

[56] ATLAS Collaboration, *The ATLAS Simulation Infrastructure*, *Eur. Phys. J.* **C 70** (2010) 823, arXiv: `1005.4568 [physics.ins-det]`.

[57] GEANT4 Collaboration, S. Agostinelli et al., *GEANT4: A simulation toolkit*, *Nucl. Instrum. Meth.* **A 506** (2003) 250.

[58] ATLAS Collaboration, *Performance of the Fast ATLAS Tracking Simulation (FATRAS) and the ATLAS Fast Calorimeter Simulation (FastCaloSim) with single particles*, 2014, URL: `http://cds.cern.ch/record/1669341`.

[59] S. Alioli et al., *A general framework for implementing NLO calculations in shower Monte Carlo programs: the POWHEG BOX*, JHEP **06** (2010) 043, arXiv: `1002.2581 [hep-ph]`.

[60] H.-L. Lai et al., *New parton distributions for collider physics*, Phys. Rev. **D 82** (2010) 074024, arXiv: `1007.2241 [hep-ph]`.

[61] P. Artoisenet et al., *Automatic spin-entangled decays of heavy resonances in Monte Carlo simulations*, JHEP **03** (2013) 015, arXiv: `1212.3460 [hep-ph]`.

[62] T. Sjöstrand, S. Mrenna and P. Z. Skands, *PYTHIA 6.4 physics and manual*, JHEP **05** (2006) 026, arXiv: `hep-ph/0603175`.

[63] J. Pumplin et al., *New generation of parton distributions with uncertainties from global QCD analysis*, *JHEP* **07** (2002) 012, arXiv: `hep-ph/0201195 [hep-ph]`.

[64] P. Z. Skands, *Tuning Monte Carlo Generators: The Perugia Tunes*, *Phys. Rev.* **D 82** (2010) 074018, arXiv: `1005.3457 [hep-ph]`.

[65] D. J. Lange, *The EvtGen particle decay simulation package*, Nucl. Instrum. Meth. **A 462** (2001) 152.

[66] M. Czakon and A. Mitov, *Top++: a program for the calculation of the top-pair cross-section at hadron colliders*, Comput. Phys. Commun. **185** (2014) 2930, arXiv: `1112.5675 [hep-ph]`.

[67] J. Alwall et al., *The automated computation of tree-level and next-to-leading order differential cross sections, and their matching to parton shower simulations*, JHEP **07** (2014) 079, arXiv: `1405.0301 [hep-ph]`.

[68] ATLAS Collaboration, *ATLAS Run 1 Pythia8 tunes*, ATL-PHYS-PUB-2014-021, 2014, URL: `https://cds.cern.ch/record/1966419`.

[69] NNPDF Collaboration, R. D. Ball et al., *Parton distributions with LHC data*, Nucl. Phys. **B 867** (2013) 244, arXiv: `1207.1303 [hep-ph]`.

[70] NNPDF Collaboration, R. D. Ball et al., *Parton distributions for the LHC run II*, Journal of High Energy Physics **2015** (2015) 1, ISSN: 1029-8479, arXiv: `1410.8849 [hep-ph]`, URL: `http://dx.doi.org/10.1007/JHEP04(2015)040`.

[71] T. Gleisberg et al., *Event generation with SHERPA 1.1*, JHEP **02** (2009) 007, arXiv: `0811.4622 [hep-ph]`.

[72] T. Gleisberg and S. Hoeche, *Comix, a new matrix element generator*, JHEP **12** (2008) 039, arXiv: `0808.3674 [hep-ph]`.

[73] F. Cascioli, P. Maierhöfer and S. Pozzorini, *Scattering Amplitudes with Open Loops*, Phys. Rev. Lett. **108** (2012) 111601, arXiv: `1111.5206 [hep-ph]`.

[74] S. Schumann and F. Krauss, *A Parton shower algorithm based on Catani-Seymour dipole factorisation*, JHEP **03** (2008) 038, arXiv: `0709.1027 [hep-ph]`.

[75] S. Hoeche et al., *QCD matrix elements + parton showers: The NLO case*, JHEP **04** (2013) 027, arXiv: `1207.5030 [hep-ph]`.

[76] ATLAS Collaboration, *Comparison of Monte Carlo generator predictions from Powheg and Sherpa to ATLAS measurements of top pair production at 7 TeV*, (2015), URL: `https://cds.cern.ch/record/2020602`.

[77] M. Bähr et al., *Herwig++ Physics and Manual*, *Eur. Phys. J.* **C 58** (2008) 639, arXiv: `0803.0883 [hep-ph]`.

[78] ATLAS Collaboration, *Multi-Boson Simulation for 13 TeV ATLAS Analyses*, ATL-PHYS-PUB-2016-002, 2016, URL: `https://cds.cern.ch/record/2119986`.

[79] ATLAS Collaboration, *Monte Carlo Generators for the Production of a W or Z/γ^* Boson in Association with Jets at ATLAS in Run 2*, ATL-PHYS-PUB-2016-003, 2016, URL: `https://cds.cern.ch/record/2120133`.

[80] ATLAS Collaboration, *Simulation of top quark production for the ATLAS experiment at $\sqrt{s}$ = 13 TeV*, ATL-PHYS-PUB-2016-004, 2016, URL: `https://cds.cern.ch/record/2120417`.

[81] ATLAS Collaboration, *Modelling of the $t\bar{t}H$ and $t\bar{t}V$ $(V = W, Z)$ processes for $\sqrt{s}$ = 13 TeV ATLAS analyses*, ATL-PHYS-PUB-2016-005, 2016, URL: `https://cds.cern.ch/record/2120826`.

[82] A. Djouadi et al., *The Minimal supersymmetric standard model: Group summary report*, (1998), arXiv: `hep-ph/9901246`.

[83] C. F. Berger, J. S. Gainer, J. L. Hewett and T. G. Rizzo, *Supersymmetry Without Prejudice*, JHEP **02** (2009) 023, arXiv: `0812.0980 [hep-ph]`.

[84] ATLAS Collaboration, *Summary of the ATLAS experiment's sensitivity to supersymmetry after LHC Run 1 — interpreted in the phenomenological MSSM*, JHEP **10** (2015) 134, arXiv: `1508.06608 [hep-ex]`.

[85] B. C. Allanach, *SOFTSUSY: a program for calculating supersymmetric spectra*, *Comput. Phys. Commun.* **143** (2002) 305, arXiv: `hep-ph/0104145`.

[86] A. Djouadi, M. Mühlleitner and M. Spira, *Decays of supersymmetric particles: The Program SUSY-HIT (SUspect-SdecaY-Hdecay-InTerface)*, Acta Phys. Polon. **B 38** (2007) 635, arXiv: `hep-ph/0609292`.

[87] W. Beenakker, R. Höpkerb, M. Spirac and P. M. Zerwas, *Squark and gluino production at hadron colliders*, Nucl.Phys. **B 492** (1997) 51, arXiv: `hep-ph/9610490 [hep-ph]`.

[88] A. Kulesza and L. Motyka, *Threshold resummation for squark-antisquark and gluino-pair production at the LHC*, *Phys. Rev. Lett.* **102** (2009) 111802, arXiv: `0807.2405 [hep-ph]`.

[89] A. Kulesza and L. Motyka, *Soft gluon resummation for the production of gluino-gluino and squark-antisquark pairs at the LHC*, *Phys. Rev.* **D 80** (2009) 095004, arXiv: `0905.4749 [hep-ph]`.

[90] W. Beenakker et al., *Soft-gluon resummation for squark and gluino hadroproduction*, JHEP **12** (2009) 041, arXiv: `0909.4418 [hep-ph]`.

[91] W. Beenakker et al., *Squark and gluino hadroproduction*, Int. J. Mod. Phys. **A 26** (2011) 2637, arXiv: `1105.1110 [hep-ph]`.

[92] M. Krämer et al., *Supersymmetry production cross sections in pp collisions at $\sqrt{s} = 7$ TeV*, (2012), arXiv: `1206.2892 [hep-ph]`.

[93] ATLAS Collaboration, *Jet energy measurement with the ATLAS detector in proton–proton collisions at $\sqrt{s} = 7$ TeV*, Eur. Phys. J. C **73** (2013) 2304, arXiv: `1112.6426 [hep-ex]`.

[94] ATLAS Collaboration, *Single hadron response measurement and calorimeter jet energy scale uncertainty with the ATLAS detector at the LHC*, Eur. Phys. J. C **73** (2013) 2305, arXiv: `1203.1302 [hep-ex]`.

[95] ATLAS Collaboration, *Jet energy resolution in proton–proton collisions at $\sqrt{s} = 7$ TeV recorded in 2010 with the ATLAS detector*, Eur. Phys. J. C **73** (2013) 2306, arXiv: `1210.6210 [hep-ex]`.

[96] ATLAS Collaboration, *Monte Carlo Calibration and Combination of In-situ Measurements of Jet Energy Scale, Jet Energy Resolution and Jet Mass in ATLAS*, ATLAS-CONF-2015-037, 2015, URL: `http://cdsweb.cern.ch/record/2044941`.

[97] M. Baak et al., *HistFitter software framework for statistical data analysis*, Eur. Phys. J. **C 75** (2015) 153, arXiv: `1410.1280 [hep-ex]`.

[98] G. Cowan et al., *Asymptotic formulae for likelihood-based tests of new physics*, Eur. Phys. J. **C71** (2011) 1554, arXiv: `1007.1727 [physics.data-an]`.

[99] A. Read, *Presentation of search results: the CL_s technique*, J. Phys. **G 28** (2002) 2693.

Appendix

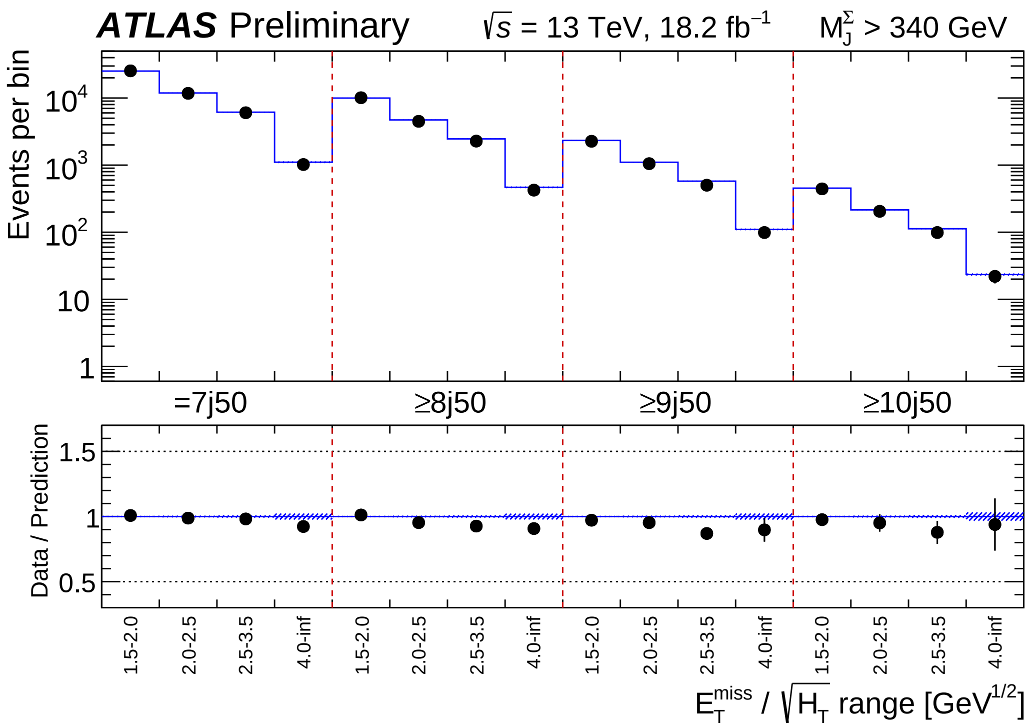

Figure 4: The degree of closure (after fitting the MC backgrounds) observed in the various multi-jet control regions for the regions with $M_J^\Sigma > 340\,\text{GeV}$. The solid lines are the predicted numbers of events and the points are the observed numbers. The signal regions are also included in the plot (4.0–inf) for 8j50, 9j50 and 10j50 however these are not included in the calculation of the systematic uncertainty. The blue uncertainty bands indicate the statistical uncertainties on the total background prediction.

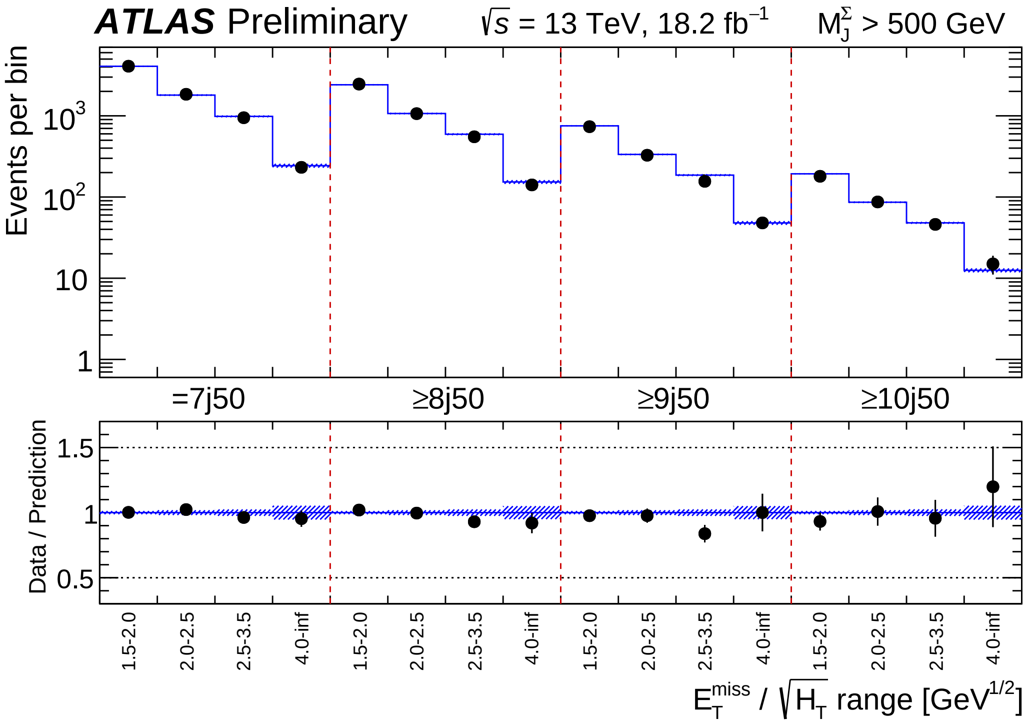

Figure 5: The degree of closure (after fitting the MC backgrounds) observed in the various multi-jet control regions for the regions with $M_J^\Sigma > 500\,\mathrm{GeV}$. The solid lines are the predicted numbers of events and the points are the observed numbers. The signal regions are also included in the plot (4.0–inf) for 8j50, 9j50 and 10j50 however these are not included in the calculation of the systematic uncertainty. The blue uncertainty bands indicate the statistical uncertainties on the total background prediction.

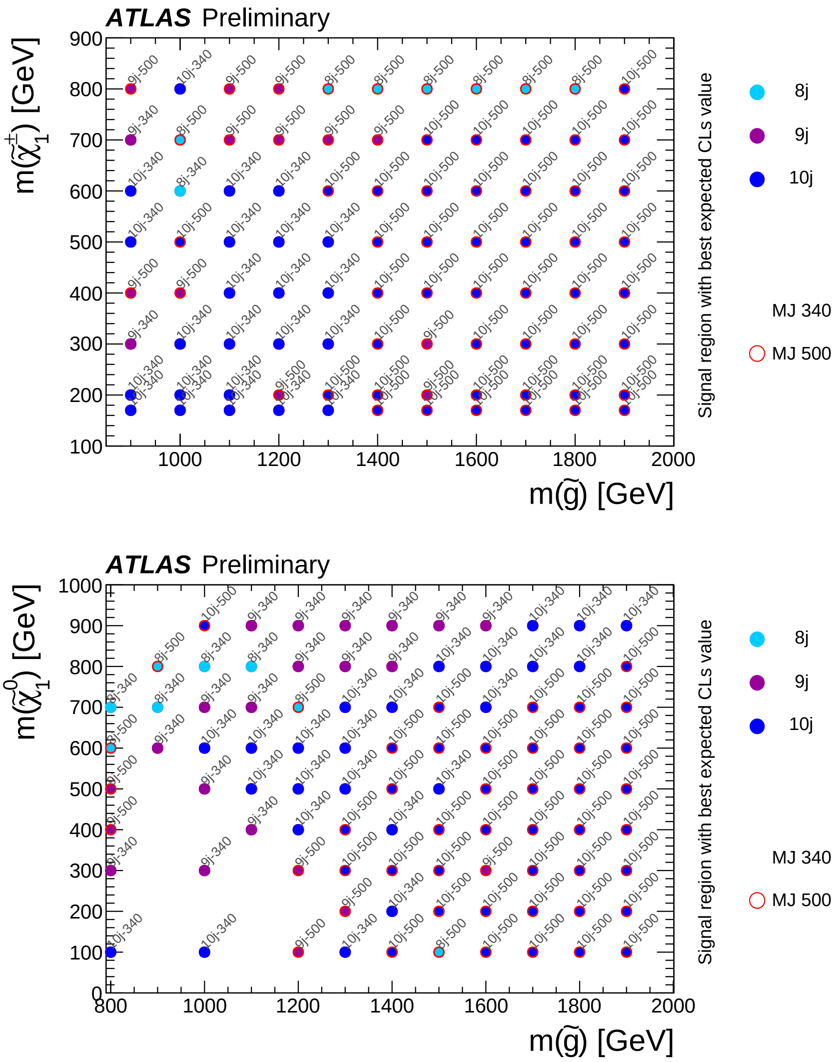

Figure 6: The signal region yielding the best-expected CLs value for each point on the pMSSM grid (top) and the 2-Step grid (bottom).